

Enhanced Photocatalytic CO₂ Reduction Activity over NH₂-MIL-125(Ti) by Facet Regulation

Xiao-Mei Cheng, Xiao-Yao Dao, Shi-Qing Wang, Jing Zhao,* and Wei-Yin Sun*

Cite This: *ACS Catal.* 2021, 11, 650–658

Read Online

ACCESS |



Metrics & More



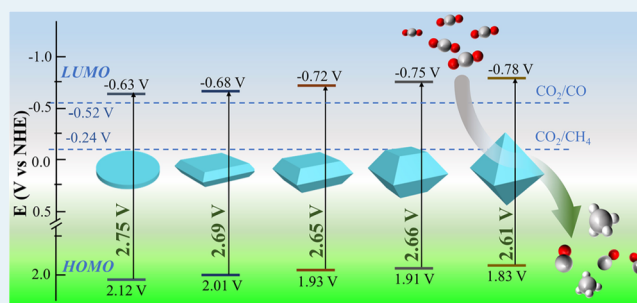
Article Recommendations



Supporting Information

ABSTRACT: Designation and optimization of facets of photocatalysts is an effective strategy to address the issue of facet-dependent photocatalytic reactions. However, studies regarding the facet effect of metal–organic frameworks (MOFs) on the photocatalytic process are in infancy. In this study, NH₂-MIL-125(Ti) with different ratios of {001} and {111} facets was exactly controlled and synthesized, and it was found that the activity in photoreduction of CO₂ is enhanced with gradually increasing exposed proportion of {111} facets. The {111} facets exhibit photocatalytic activity with the maximal CO and CH₄ yields of 8.25 and 1.01 μmol g⁻¹ h⁻¹, which are 9 and 5 times higher than those of {001} facets, respectively. Also, the {111} facets give the highest quantum yields of 0.14 and 0.07% for CO and CH₄ production, respectively. Steady-state and time-resolved fluorescence spectra reveal the importance of inhibiting the recombination of photoinduced electrons and holes for the sample with {111} facets. Besides, Ti^{III} formed during the reaction process exhibits strong reducibility for CO₂. Starting from NH₂-MIL-125(Ti), the photocatalytic performance can be enhanced by regulating exposed {111} facets. This work not only provides a strategy for further enhancing photocatalytic performance by tuning the exposed active facets of MOFs, but also provides a deep understanding of the factors for improving the photocatalytic reduction of CO₂.

KEYWORDS: NH₂-MIL-125(Ti), facets, metal–organic frameworks, CO₂ reduction, photocatalytic reaction



1. INTRODUCTION

Photoreduction of CO₂ to generate valuable fuels and chemical feedstocks is considered as an effective way to alleviate the greenhouse effect and address the energy issues.^{1–3} However, the inertness of the CO₂ molecule and inherent defects of the photocatalyst lead to low efficiency of photocatalytic CO₂ reduction.^{4–6} To overcome these drawbacks, enormous efforts have been made for metal–organic frameworks (MOFs) to improve the activity of photoreduction of CO₂, including heterojunction construction, cocatalyst loading, and surface engineering.^{7–11} Owing to the catalytic reactions that mainly occur on the surface of the catalysts, the optical and chemical properties of catalysts are largely dependent on the degree of exposed facets.^{12–14} Also, the optimization of surface structure is favor of electron generation and spatial separation, which are crucial for photoreduction of CO₂.^{15–17} Thus, we focus our attention on exploring the regulation of the surface facet of MOFs and its influence on the activity of CO₂ photoreduction.¹⁸

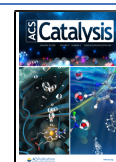
MOFs, as a type of inorganic–organic hybrid materials with a high surface area, tunable porosity, and tailorable structure, show definite advantages concerning the capability of precisely designed and optimized surface structure.^{19–24} There are reports about morphology and facet control of MOFs in the

past decades, which provided supports for our work.^{25–27} Particularly, the titanium-based MOF, NH₂-MIL-125(Ti) with high chemical stability and significant optical response, is one of the most efficient photocatalysts for H₂ generation, organic pollutant degradation, and CO₂ photoreduction.^{28–31} To improve the photocatalytic efficiency of NH₂-MIL-125(Ti), the common way is to load cocatalysts, such as noble metals, inorganic semiconductors, and functional materials.^{32,33} For example, amorphous TiO₂-decorated NH₂-MIL-125(Ti) composites enhanced the activity of photocatalytic CO₂ to CH₄ conversion, which was 1.7 times higher than that of pure NH₂-MIL-125(Ti).³⁴ Composite photocatalyst g-C₃N₄/CuO@NH₂-MIL-125(Ti) achieved by encapsulating CuO quantum dots and combining with g-C₃N₄ exhibits remarkably improved activity of CO₂ photoreduction and charge separation efficiency.³⁵

Received: October 12, 2020

Revised: December 17, 2020

Published: December 30, 2020



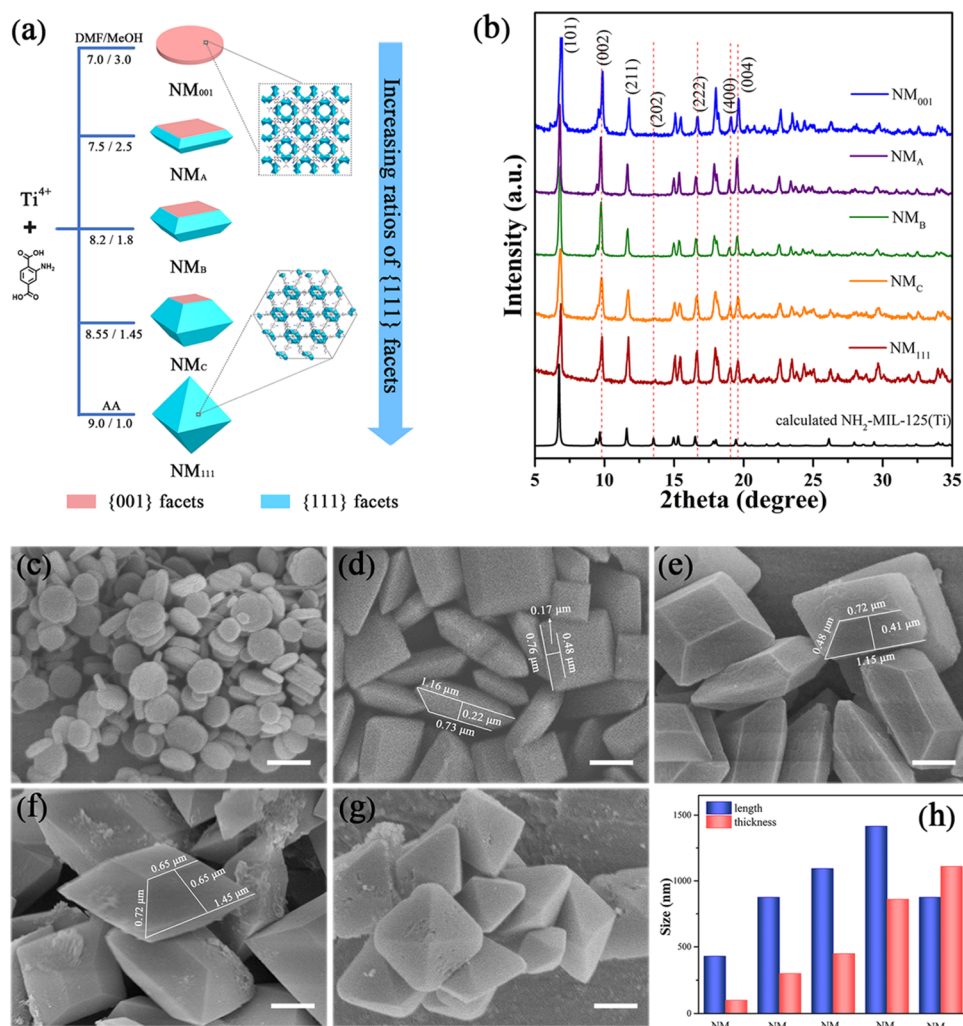


Figure 1. (a) Schematic illustration of the evolution of morphology and facet over $\text{NH}_2\text{-MIL-125}(\text{Ti})$. (b) PXRD patterns of as-synthesized photocatalysts and calculated $\text{NH}_2\text{-MIL-125}(\text{Ti})$. SEM spectra of NM₀₀₁ (c), NM_A (d), NM_B (e), NM_C (f), and NM₁₁₁ (g) and average sizes (h) of as-synthesized $\text{NH}_2\text{-MIL-125}(\text{Ti})$. Scale bar: 500 nm.

Herein, we report $\text{NH}_2\text{-MIL-125}(\text{Ti})$ for photoreduction of CO_2 focused on the impact of facet regulation for photocatalytic activity. The {001}, {111}, and co-exposed {001} and {111} facets of $\text{NH}_2\text{-MIL-125}(\text{Ti})$ were successfully fabricated with morphologies of disk, octahedron, and truncated octahedrons, respectively. They exhibit excellent photoreduction activity for CO_2 to CO and CO_2 to CH_4 conversion. Importantly, the {111} facets possess a large specific surface area and superior CO_2 uptake, which provide more active sites for the reduction reaction. Likewise, the content of Ti atoms in {111} facets is higher than that in {001} facets, Ti^{III} in favor of accelerating the progress of reduction reaction by unveiling more active sites during the reaction process. The {111} facets exhibit optimal photocatalytic activity for CO_2 reduction ascribed to the fast electron transfer and effectively suppressed recombination of electron–hole pairs. Besides, regulating the active facets is beneficial to broaden the absorption range, reconstruct the electronic structure, and prolong the lifetimes of photogenerated electrons of $\text{NH}_2\text{-MIL-125}(\text{Ti})$.

2. EXPERIMENTAL SECTION

2.1. Preparation of $\text{NH}_2\text{-MIL-125}(\text{Ti})$ with Different Exposed Facets.

In a typical experiment, $\text{NH}_2\text{-BDC}$ and

modulator (acetic acid, AA) were dissolved in MeOH and DMF mixture solution to a total volume of 10 mL. Then, a titanium source was added and mixed with sonication for 5 min. The specific amounts of reactants and modulators in the synthesis are presented in Table S1 (see the [Supporting Information](#)). The obtained solution was transferred into the Teflon-line steel autoclave and kept in an oven at 150 °C for 24 h. The yellow powders were isolated by centrifugation, thoroughly washed with DMF and MeOH several times, and dried under vacuum for 5 h at 80 °C.

3. RESULTS AND DISCUSSION

In the synthetic system, we identified that the volume ratio of DMF and MeOH is powerful to adjust the ratio of {001} and {111} facets. These samples are denoted as NM₀₀₁, NM_A, NM_B, NM_C, and NM₁₁₁, where NM represents $\text{NH}_2\text{-MIL-125}(\text{Ti})$; 001 and 111 are the dominant facets; and A, B, and C are the mixed {001} and {111} facets with different ratios. Tuning the solvent ratio of DMF and MeOH and different titanium sources of titanium tetraisopropanolate (TPOT) or titanium butoxide (TBOT) with or without a modulator of AA can achieve transition of the morphology and facet for $\text{NH}_2\text{-MIL-125}(\text{Ti})$ (Figure 1a). For further observation of the

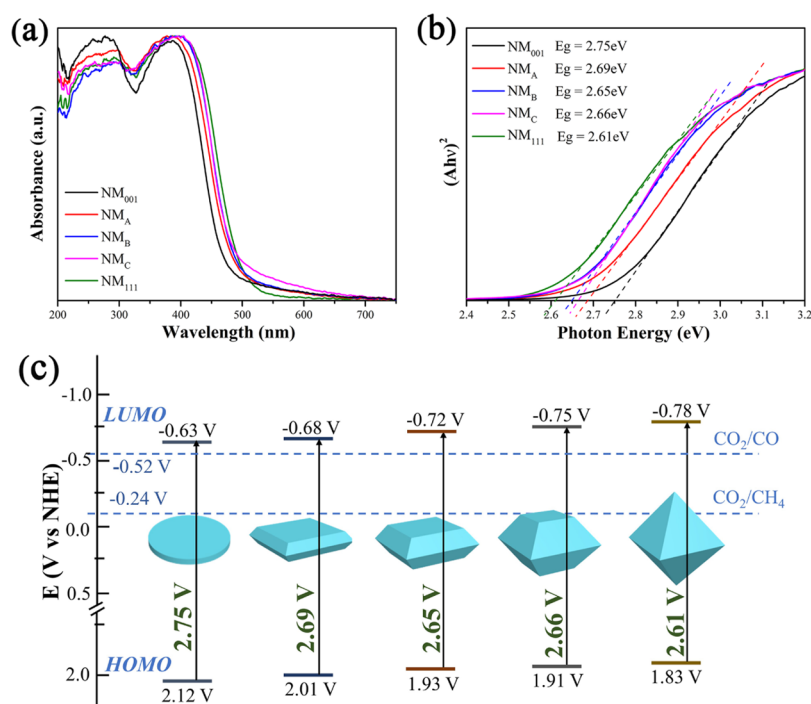


Figure 2. (a) UV-vis diffuse reflectance spectra, (b) Tauc plots, and (c) HOMO-LUMO gap of the as-synthesized photocatalysts.

evolution of the morphology and facet of all samples directly, scanning electron microscopy (SEM) images were obtained. Clearly, these well-faceted NH₂-MIL-125(Ti) can be easily identified as {001} and {111} facets according to the SEM. The disk-shaped NH₂-MIL-125(Ti) exposes two {001} facets on the top and bottom (Figure 1c). Along with the variation of tuning factors (Table S1), the {001} facets are gradually diminished, and the {111} facets appeared and increased (Figure 1d–f). Until the last sample shown in Figure 1g, {001} facets disappeared, and the {111} facets were exposed completely. The results demonstrate the evolution of as-synthesized NH₂-MIL-125(Ti) facets from {001} to {111}. The average sizes of the samples are displayed in Figure 1h. The average percentages of exposed {001} and {111} facets were calculated from the corresponding facet area as illustrated in Scheme S1 (Table S3).³⁶

Powder X-ray diffraction (PXRD) patterns of the as-synthesized samples are shown in Figure 1b, which confirm that all the samples matched well with the calculated NH₂-MIL-125(Ti).³⁷ It is noteworthy that the relative intensity of (101) and (202) crystallographic planes at 6.7 and 13.5° reduced and disappeared, respectively. Furthermore, compared with the calculated NH₂-MIL-125(Ti), the relative intensity of (222) facet at 16.6° increased gradually from NM₀₀₁ to NM₁₁₁. The (*hkl*) denotes Miller indices of the facet, and {*hkl*} indicates a family index of the crystal facet.³⁸ XRD peaks reflect the distribution of atom arrays in the facet of samples, and facet-dependent PXRD patterns indicate that the surfaces of NM₀₀₁ and NM₁₁₁ are dominated by {001} and {111} facets, respectively, as discussed previously.²⁸ The facet-dependent PXRD patterns are consistent with the morphology and facet observed by SEM. The Fourier transform infrared (FT-IR) spectra are shown in Figure S1 to further clarify the functional groups of NH₂-MIL-125(Ti). Thermogravimetric analyses reveal that NH₂-MIL-125(Ti) with different exposed facets have similar thermal stability (Figure S2). These character-

izations indicate that NH₂-MIL-125(Ti) with varied proportions of exposed {001} and {111} facets were successfully achieved.

To investigate the optical properties of these samples, UV-vis diffuse reflectance spectra were examined. The results indicate that all samples display light absorption from the UV to visible region (Figure 2a). The prepared samples mainly exhibit two absorption bands around 300 and 400 nm, corresponding to the absorption of Ti–O_x clusters and ligand-based absorption within the framework of MOFs.^{35,39} The absorption wavelength shows red shift with increasing the ratios of {111} facets of the samples. The NM₁₁₁ displays the maximal red-shifted absorption wavelength, while NM₀₀₁ gives the narrowest absorption. Tauc plots were used to estimate the highest occupied molecular orbital (HOMO)–lowest unoccupied molecular orbital (LUMO) gap, as depicted in Figure 2b. For semiconductor-like MOFs, the HOMO–LUMO gap is defined as the gap between the HOMO and the LUMO according to the molecular orbital model. To estimate the HOMO–LUMO gap edges of the catalysts, the Mott–Schottky plots were measured (Figures S3–S7). The flat band potentials were determined to be –0.63, –0.68, –0.72, –0.75, and –0.78 V versus NHE for NM₀₀₁, NM_A, NM_B, NM_C, and NM₁₁₁, respectively. Thus, the calculated HOMO–LUMO gaps are 2.75 eV (NM₀₀₁), 2.69 eV (NM_A), 2.65 eV (NM_B), 2.66 eV (NM_C), and 2.61 eV (NM₁₁₁), as shown in Figure 2c. The catalyst with a lower HOMO–LUMO gap requires light with lower energy to inspire photogenerated electrons and holes. Accordingly, the exposure of {111} facets in NH₂-MIL-125(Ti) is favorable for possessing a better photoresponse under simulated sunlight irradiation and decreasing the energy of photoexcited electrons.

According to the optical behavior of these samples, we explored their photocatalytic performance for CO₂ reduction and evaluated the correlation between photocatalytic activity and facets of the as-synthesized NH₂-MIL-125(Ti). The

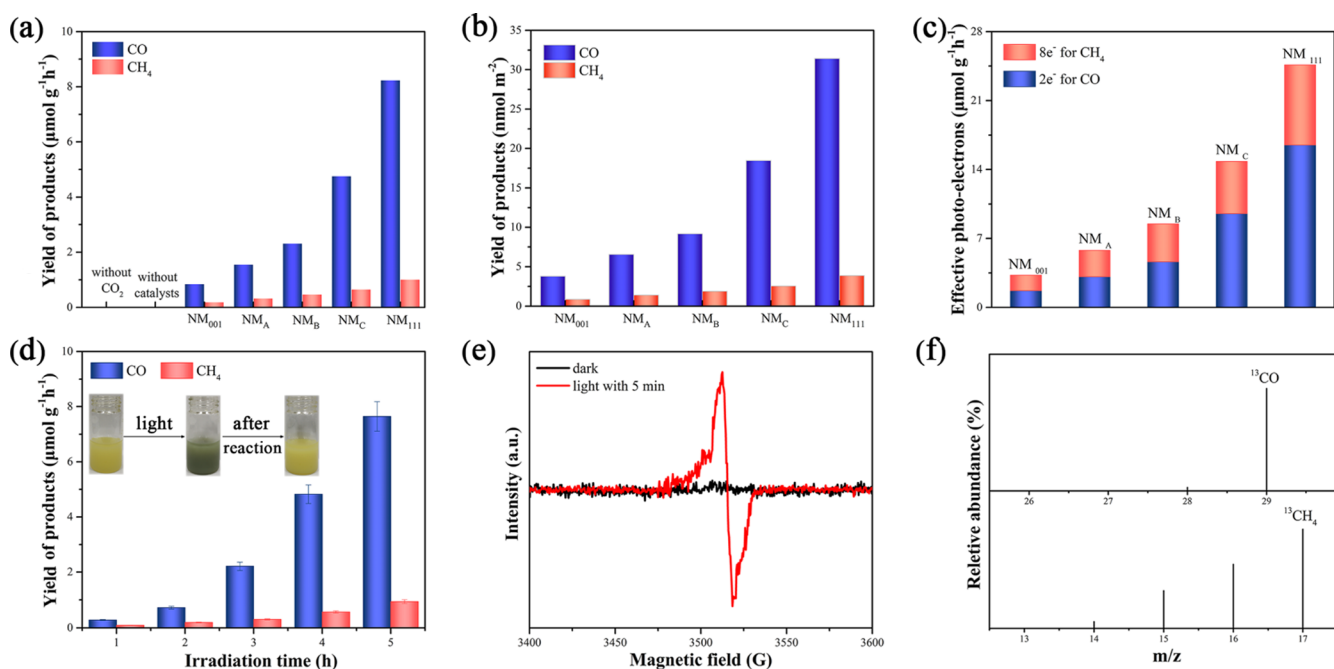


Figure 3. Yields of products with respect to the mass of catalysts (a) and with respect to the facet surface area (b), effective photoelectrons of CO and CH₄ under visible light irradiation (5 h) of the as-synthesized photocatalysts (c), irradiation time-dependence evolution of CO and CH₄ of NM₁₁₁ (d), EPR spectra of NM₁₁₁ in the dark and upon irradiation for 5 min (e), mass spectral analysis for photoreduction of ¹³CO₂ to ¹³CO ($m/z = 29$) and ¹³CH₄ ($m/z = 17$) using NM₁₁₁ as the photocatalyst (f).

photocatalytic CO₂-to-CO and CO₂-to-CH₄ conversions of the samples are depicted in Figure 3a. The CO and CH₄ characterized peaks are monitored by an FID detector (Figure S8). The NM₁₁₁ exhibits superior photocatalytic activity for generation of CO and CH₄ with product yields of 8.25 and 1.01 $\mu\text{mol g}^{-1}\text{h}^{-1}$, which are 9 and 5 times higher than those of NM₀₀₁, respectively. Also, NM₁₁₁ gives the highest quantum yields (QYs) of 0.14 and 0.07% for CO and CH₄ production (Table S4), which are comparable or higher than some reported photocatalysts (Tables S5 and S6). Interestingly, the trend of the product yields with respect to the facet surface area is consistent with the mass of catalysts (Figure 3a,b), and NM₁₁₁ shows the best performance (Figure 3b).^{40,41} Upon irradiation, the reduction reaction proceeded, in which TEOA acts as a proton and electron donor, providing 2e⁻ and 8e⁻ for reduction products of CO and CH₄, respectively (Figure 3c). The degradation product of TEOA is determined as 2-(bis(2-hydroxyethyl)amino)acetaldehyde (Figures S9 and S10). The ¹H NMR spectrum is used to prove that no liquid product was generated during the photocatalytic reaction (Figure S11). To verify that the detected CO and CH₄ are generated via the photocatalytic CO₂ reduction, we performed comparison experiments. No C₁ products can be detected with absent CO₂ or photocatalyst. To further confirm the carbon source of the CO and CH₄ products, the ¹³C-isotope trace experiment was employed using ¹³CO₂ as the substrate. The products were analyzed by gas chromatography–mass spectrometry (GC–MS). The signal peaks at $m/z = 29$ (¹³CO) and $m/z = 17$ (¹³CH₄) are observed (Figure 3f). The irradiation time-dependence evolution of CO and CH₄ during 5 h is given in Figure 3d, and the intriguing phenomenon of the photochromic effect was observed in this photocatalytic system (inset in Figure 3d). The color changed from original bright yellow to green with constant irradiation and then turned to the yellow after the photocatalytic reaction. This process is

attributed to the interconversion between Ti^{IV} and Ti^{III} valent states in the Ti–O_x cluster with transition of the photo-generated electrons.⁴² Furthermore, electron paramagnetic resonance (EPR) spectra were measured to elucidate the existence of Ti^{III}. As revealed in Figure 3e, no EPR signal was detected in the dark, while an obvious peak was observed with a *g* factor of 1.948 upon irradiation for 5 min.^{43,44} The results provide clues to further ensure the existence of Ti^{III}, indicating the conversion of Ti^{IV} to Ti^{III} in the photoreduction system. It is noteworthy that NM₁₁₁ exhibits excellent stability after five cycles, and the photoreduction activity was maintained above 85% compared with the initial test (Figure S12). The PXRD pattern (Figure S13), FT-IR spectra (Figure S14), and SEM image (Figure S15) of NM₁₁₁ after five recycles confirm the structure stability under the photocatalytic reaction conditions.

To further explore the facet effect on the photocatalytic CO₂ reduction, N₂ adsorption isotherms were measured to obtain specific surface areas of the as-synthesized samples. As shown in Figure S16, all samples exhibit type I isotherms at 77 K with strong N₂ uptakes at a low relative pressure ($P/P_0 < 0.001$).^{45,46} NM₁₁₁ possesses the largest specific surface area (1312.2 cm^2g^{-1}) among all the samples. The specific surface areas are found to increase with the increasing percentages of exposed {111} facets. Moreover, the adsorption abilities of these photocatalysts were investigated with catalytic substrate CO₂, and CO₂ adsorption isotherms are obtained at 273 (Figure S17) and 298 K (Figure S18), showing the relatively large amounts CO₂ uptakes of NM₁₁₁. The specific surface areas and the CO₂ uptakes are listed in Table S3. The high specific surface area and superior CO₂ uptake ability of NM₁₁₁ provide more active sites for enhanced photocatalytic CO₂ reduction activity.⁴⁷

The survey spectra of X-ray photoelectron spectroscopy (XPS) are provided in Figure S19, and high-resolution XPS (HR–XPS) was employed to estimate the chemical state and

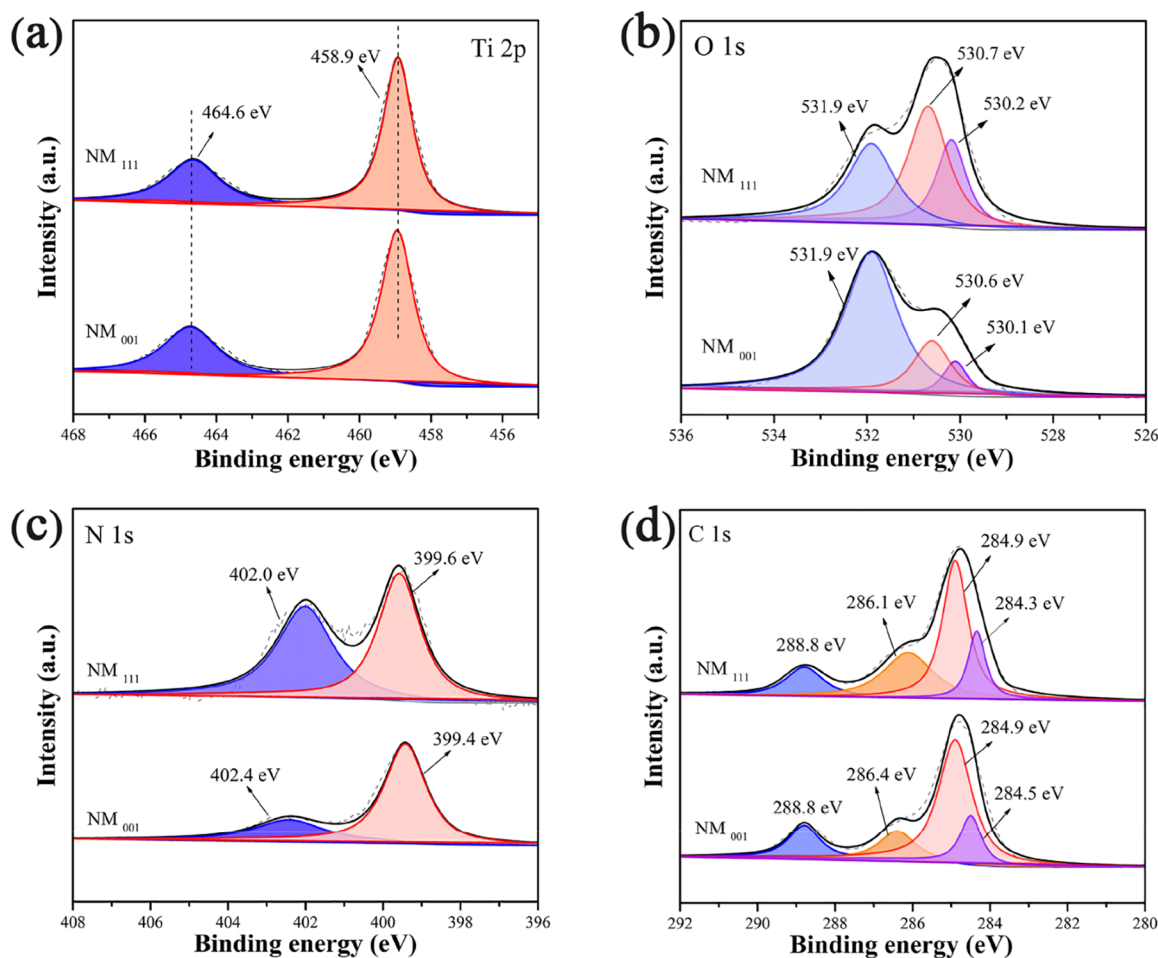


Figure 4. HR-XPS spectra of Ti 2p (a), O 1s (b), N 1s (c), and C 1s (d) of NM_{111} and NM_{001} .

coordination environment of NM_{111} and NM_{001} . As shown in Figure 4a, the Ti 2p displays two binding energy peaks at 458.9 and 464.6 eV, which is attributed to Ti 2p_{3/2} and Ti 2p_{1/2} of Ti^{IV}, respectively, indicating that titanium bonded to oxygen in the Ti–O_x cluster remained in Ti^{IV}.⁴⁸ High-resolution O 1s presents distinction between NM_{111} and NM_{001} with three fitted peaks (Figure 4b). The first peak located at 531.9 eV is assigned to the oxygen in the carboxylate group in NH₂-BDC, while the other two peaks at 530.7 and 530.2 eV are ascribed to oxygen in the Ti–O_x cluster of NM_{111} .⁴⁹ The observed peak intensities are clearly higher than those of NM_{001} , indicating that more Ti–O_x clusters are exposed in the {111} facets in NM_{111} . The atomic concentrations of NM_{111} and NM_{001} are listed in Table S2. NM_{111} exhibits higher Ti atomic concentration than NM_{001} , demonstrating more exposure of Ti–O_x clusters on the surface of NM_{111} . The structure of {001} and {111} facets in NH₂-MIL-125(Ti) revealed the distinct distribution of Ti–O_x on different facets (Figures S20 and S21). As shown in Figure 4c, high-resolution N 1s presents two peaks corresponding to the –NH–⁺ and –NH₂ in amino groups of NM_{111} and NM_{001} , respectively.⁵⁰ Obviously, the binding energy at 402.0 eV of NM_{111} is stronger than that of NM_{001} , implying the stronger electron transfer in NM_{111} . The results demonstrate abundant Ti–O_x clusters and the vigorous electron transfer on the surface of NM_{111} , which further improve the photocatalytic activity.

In addition to UV–vis spectra, steady photoluminescence (PL) spectral measurements were carried out to in-depth

investigate photoinduced charge separation properties (Figure 5a). Under the excitation wavelength of 325 nm, NM_{001} shows a high-intensity fluorescence at 485 nm due to the fast recombination of charge carriers, while PL intensity decreased significantly with the increase of the percentages of the {111} facets. Such appearance indicates the low recombination rate of photoinduced charge carriers and the effective separation of photogenerated electrons and holes in {111} facets. The time-resolved fluorescence decay spectra were performed to explore the photogenerated carrier dynamics of these as-synthesized photocatalysts (Figure 5b). The charge-separated lifetime increases in the order of NM_{001} (0.17 ns) < NM_A (0.94 ns) < NM_B (1.19 ns) < NM_C (1.25 ns) < NM_{111} (1.63 ns), generally corresponding to a trend of prolonged lifetimes with the increase in the exposure of {111} facets. In the present case, the longer fluorescence lifetimes are attributed to the fast transfer of photoinduced charge carriers and inhibition of the recombination of photogenerated electrons and holes.⁵¹ The effective electronic interactions among these photocatalysts were investigated by the photocurrent transient response measurement (Figure 5c). All the catalysts exhibited a clear photocurrent response under on–off simulated sunlight irradiation. NM_{001} shows lower photocurrent density due to the fast recombination of photogenerated charge carriers. The photocurrent signal increases with the increase of the ratio of exposed {111} facets, and NM_{111} possesses the largest photocurrent response, revealing that the NM_{111} has capability of interface charge transfer and separation. Besides, the results

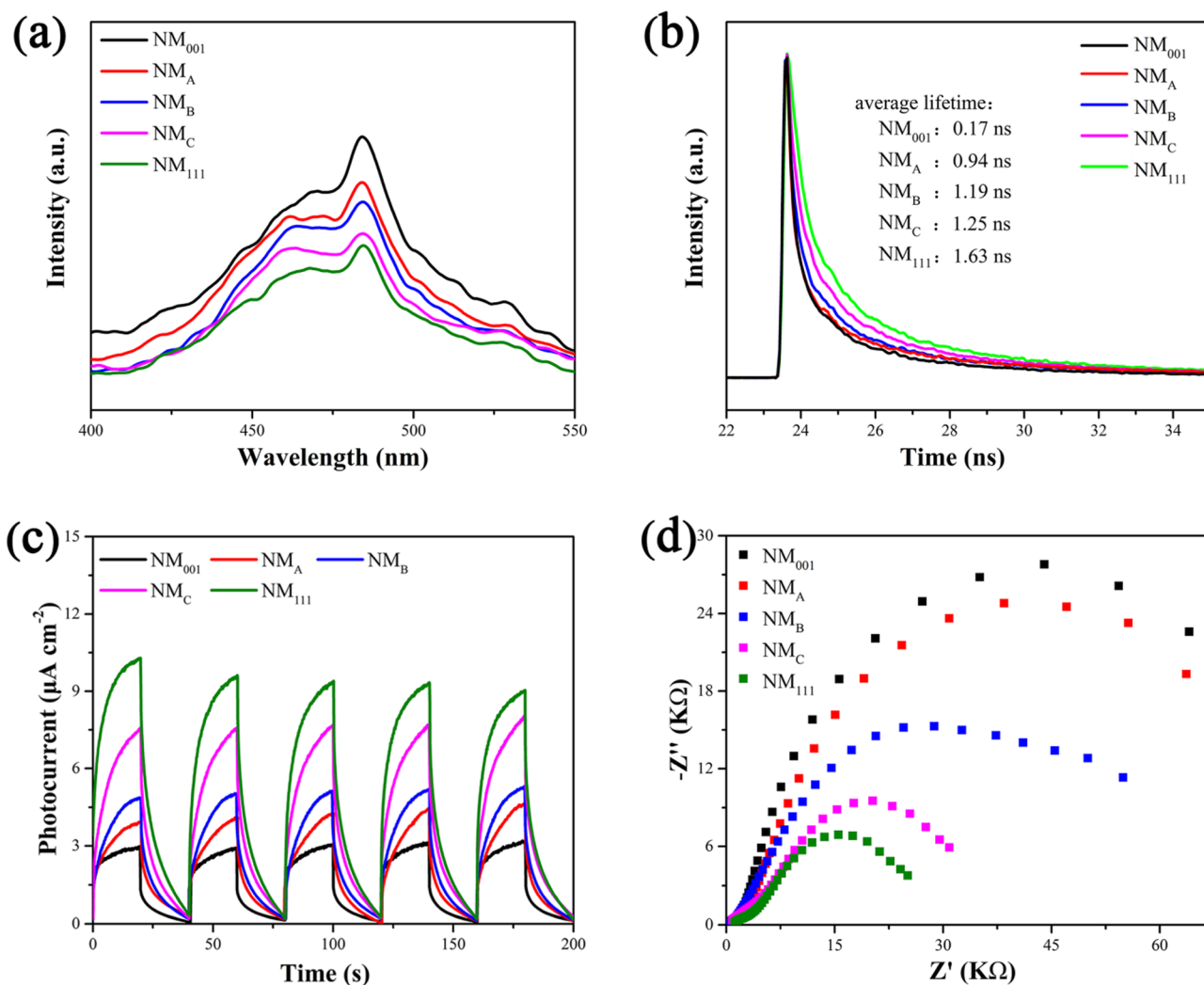
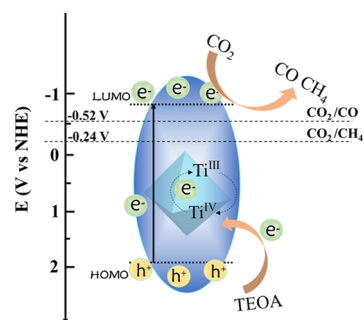


Figure 5. (a) Steady photoluminescence spectra under 325 nm excitation, (b) time-resolved fluorescence decay spectra, (c) photocurrent transient response, and (d) EIS Nyquist plots of the as-synthesized photocatalysts.

are also supported by electrochemical impedance spectroscopy (EIS) (Figure 5d). The charge transfer resistance (R_{ct}) of NM_{111} is much lower than that of NM_{001} , NM_A , NM_B , and NM_C , indicating the favorable electron transfer of NM_{111} during the light irradiation.

Based on the above results, we proposed a possible mechanism for enhancing the photocatalytic activity of CO_2 reduction of NH_2 -MIL-125(Ti) with exposed varied ratios of {001} and {111} facets (Scheme 1). First, the high LUMO value of NM_{111} reaches -0.78 V (vs NHE) with a strong ability to realize CO_2 -to- CO (-0.52 V) and CO_2 -to- CH_4 (-0.24 V) conversions.^{17,52} Photogenerated electrons are excited from the HOMO under simulated light irradiation owing to the lower HOMO–LUMO gap and then migrate to LUMO to trigger the reduction reaction, while the photogenerated holes participate in the oxidation reaction. Second, TEOA as a sacrificial agent in this photocatalytic system will be oxidized, providing electrons to the photocatalytic system in the meantime. Third, high specific surface area and superior CO_2 uptake ability provide efficient active sites. Ti^{IV} in the NH_2 -MIL-125(Ti) captures the electron and converts to Ti^{III} , and the Ti^{III} sites possess strong reducibility to realize the conversion of CO_2 to the CO and CH_4 products. The NM_{111} photocatalyst effectively suppresses the recombination

Scheme 1. Proposed Mechanism of NM_{111} for Photoreduction CO_2 to CO and CH_4



of photogenerated electrons and holes. Thus, a lot of electrons and holes participate in the photocatalytic reaction and further promote the photocatalytic activity of CO_2 reduction.

4. CONCLUSIONS

In summary, we accurately designed and successfully synthesized a series of NH_2 -MIL-125(Ti) with varied ratios of {111} facets by one-step solvothermal method, achieving the exact control of active exposed facets and comprehensively

evaluating the ability of photocatalytic CO₂ reduction of the as-synthesized photocatalysts. We also realized the optimization of CO₂ photoreduction activity with 100% exposure of {111} facets. The enhanced photoreduction of CO₂ activity was attributed to the exposure of {111} facets, which not only enlarge the specific surface area and CO₂ adsorption, prolong the PL lifetime, and increase the Ti atomic concentrations but also rapidly spatially separate and effectively suppress the recombination of electrons and holes. The transition between Ti^{IV} and Ti^{III} has been considered in the photoreaction, which facilitated the photoreduction process and enhanced photocatalytic activity. The NM₁₁₁ sample could be readily achieved by solvothermal reaction, and further efforts are needed to enhance the activity by incorporating composite species and/or optimize the CO₂ reduction product such as CH₄. This work demonstrates the intriguing investigation of the facet effect of NH₂-MIL-125(Ti), which paves new ways for designing efficient MOF catalysts for photocatalytic performance by regulating the exposed active facets. The challenges in exploring the facet effect in MOFs still remain, and more efforts may be required in the future.

■ ASSOCIATED CONTENT

SI Supporting Information

The Supporting Information is available free of charge at <https://pubs.acs.org/doi/10.1021/acscatal.0c04426>.

FT-IR, TG, Mott–Schottky plots, ESI–MS, NMR, SEM images, PXRD, N₂ and CO₂ adsorption, XPS, structures, synthetic system, atomic concentration facet ratio, QY, and comparison of photocatalytic CO₂ reduction (PDF)

■ AUTHOR INFORMATION

Corresponding Authors

Jing Zhao – State Key Laboratory of Coordination Chemistry, Chemistry and Biomedicine Innovation Center (ChemBIC), School of Chemistry and Chemical Engineering, Nanjing University, Nanjing 210023, China; orcid.org/0000-0001-5177-5699; Email: jingzhao@nju.edu.cn

Wei-Yin Sun – Coordination Chemistry Institute, State Key Laboratory of Coordination Chemistry, School of Chemistry and Chemical Engineering, Nanjing National Laboratory of Microstructures, Collaborative Innovation Center of Advanced Microstructures, Nanjing University, Nanjing 210023, China; orcid.org/0000-0001-8966-9728; Email: sunwy@nju.edu.cn

Authors

Xiao-Mei Cheng – Coordination Chemistry Institute, State Key Laboratory of Coordination Chemistry, School of Chemistry and Chemical Engineering, Nanjing National Laboratory of Microstructures, Collaborative Innovation Center of Advanced Microstructures, Nanjing University, Nanjing 210023, China; State Key Laboratory of Coordination Chemistry, Chemistry and Biomedicine Innovation Center (ChemBIC), School of Chemistry and Chemical Engineering, Nanjing University, Nanjing 210023, China

Xiao-Yao Dao – Coordination Chemistry Institute, State Key Laboratory of Coordination Chemistry, School of Chemistry and Chemical Engineering, Nanjing National Laboratory of Microstructures, Collaborative Innovation Center of

Advanced Microstructures, Nanjing University, Nanjing 210023, China

Shi-Qing Wang – Coordination Chemistry Institute, State Key Laboratory of Coordination Chemistry, School of Chemistry and Chemical Engineering, Nanjing National Laboratory of Microstructures, Collaborative Innovation Center of Advanced Microstructures, Nanjing University, Nanjing 210023, China

Complete contact information is available at: <https://pubs.acs.org/10.1021/acscatal.0c04426>

Notes

The authors declare no competing financial interest.

■ ACKNOWLEDGMENTS

We gratefully acknowledge the National Basic Research Program of China (grant no. 2017YFA0303504) and the Fundamental Research Funds for the Central Universities (grant no. 14380232) for financial support of this work. This work was also supported by a Project Funded by the Priority Academic Program Development of Jiangsu Higher Education Institutions.

■ REFERENCES

- (1) Wu, Y. A.; McNulty, I.; Liu, C.; Lau, K. C.; Liu, Q.; Paulikas, A. P.; Sun, C.-J.; Cai, Z.; Guest, J. R.; Ren, Y.; Stamenkovic, V.; Curtiss, L. A.; Liu, Y.; Rajh, T. Facet-Dependent Active Sites of a Single Cu₂O Particle Photocatalyst for CO₂ Reduction to Methanol. *Nat. Energy* **2019**, *4*, 957–968.
- (2) Lin, L.; Lin, Z.; Zhang, J.; Cai, X.; Lin, W.; Yu, Z.; Wang, X. Molecular-Level Insights on the Reactive Facet of Carbon Nitride Single Crystals Photocatalysing overall Water Splitting. *Nat. Catal.* **2020**, *3*, 649–655.
- (3) Wang, S.; Liu, G.; Wang, L. Crystal Facet Engineering of Photoelectrodes for Photoelectrochemical Water Splitting. *Chem. Rev.* **2019**, *119*, 5192–5247.
- (4) Wang, Y.; Liu, X.; Zheng, C.; Li, Y.; Jia, S.; Li, Z.; Zhao, Y. Tailoring TiO₂ Nanotube-Interlaced Graphite Carbon Nitride Nanosheets for Improving Visible-Light-Driven Photocatalytic Performance. *Adv. Sci.* **2018**, *5*, 1700844–1700852.
- (5) Remiro-Buenamañana, S.; Cabrero-Antonino, M.; Martínez-Guante, M.; Álvaro, M.; Navalón, S.; García, H. Influence of Cocatalysts on the Photocatalytic Activity of MIL-125(Ti)-NH₂ in the overall Water Splitting. *Appl. Catal., B* **2019**, *254*, 677–684.
- (6) Zhang, H. X.; Hong, Q. L.; Li, J.; Wang, F.; Huang, X.; Chen, S.; Tu, W.; Yu, D.; Xu, R.; Zhou, T.; Zhang, J. Isolated Square-Planar Copper Center in Boron Imidazolate Nanocages for Photocatalytic Reduction of CO₂ to CO. *Angew. Chem., Int. Ed.* **2019**, *58*, 11752–11756.
- (7) Zhao, L.; Zhao, Z.; Li, Y.; Chu, X.; Li, Z.; Qu, Y.; Bai, L.; Jing, L. The Synthesis of Interface-Modulated Ultrathin Ni(II) MOF/g-C₃N₄ Heterojunctions as Efficient Photocatalysts for CO₂ Reduction. *Nanoscale* **2020**, *12*, 10010–10018.
- (8) Feng, X.; Pi, Y.; Song, Y.; Brzezinski, C.; Xu, Z.; Li, Z.; Lin, W. Metal-Organic Frameworks Significantly Enhance Photocatalytic Hydrogen Evolution and CO₂ Reduction with Earth-Abundant Copper Photosensitizers. *J. Am. Chem. Soc.* **2020**, *142*, 690–695.
- (9) Deng, X.; Yang, L.; Huang, H.; Yang, Y.; Feng, S.; Zeng, M.; Li, Q.; Xu, D. Shape-Defined Hollow Structural Co-MOF-74 and Metal Nanoparticles@Co-MOF-74 Composite Through a Transformation Strategy for Enhanced Photocatalysis Performance. *Small* **2019**, *15*, 1902287–1902294.
- (10) Chen, L.; Wang, Y.; Yu, F.; Shen, X.; Duan, C. A Simple Strategy for Engineering Heterostructures of Au Nanoparticle-Loaded Metal-Organic Framework Nanosheets to Achieve Plasmon-Enhanced

Photocatalytic CO₂ Conversion under Visible Light. *J. Mater. Chem. A* **2019**, *7*, 11355–11361.

(11) Ran, J.; Jaroniec, M.; Qiao, S.-Z. Cocatalysts in Semiconductor-Based Photocatalytic CO₂ Reduction: Achievements, Challenges, and Opportunities. *Adv. Mater.* **2018**, *30*, 1704649.

(12) Mu, L.; Zhao, Y.; Li, A.; Wang, S.; Wang, Z.; Yang, J.; Wang, Y.; Liu, T.; Chen, R.; Zhu, J.; Fan, F.; Li, R.; Li, C. Enhancing Charge Separation on High Symmetry SrTiO₃ Exposed with Anisotropic Facets for Photocatalytic Water Splitting. *Energy Environ. Sci.* **2016**, *9*, 2463–2469.

(13) Pan, J.; Liu, G.; Lu, G. Q. M.; Cheng, H.-M. On the True Photoreactivity Order of {001}, {010}, and {101} Facets of Anatase TiO₂ Crystals. *Angew. Chem., Int. Ed.* **2011**, *50*, 2133–2137.

(14) Sun, S.; Gao, P.; Yang, Y.; Yang, P.; Chen, Y.; Wang, Y. N-Doped TiO₂ Nanobelts with Coexposed (001) and (101) Facets and Their Highly Efficient Visible-Light-Driven Photocatalytic Hydrogen Production. *ACS Appl. Mater. Interfaces* **2016**, *8*, 18126–18131.

(15) Li, R.; Zhang, W.; Zhou, K. Metal-Organic-Framework-Based Catalysts for Photoreduction of CO₂. *Adv. Mater.* **2018**, *30*, 1705512–1705542.

(16) Dao, X.-Y.; Guo, J.-H.; Wei, Y.-P.; Guo, F.; Liu, Y.; Sun, W.-Y. Solvent-Free Photoreduction of CO₂ to CO Catalyzed by Fe-MOFs with Superior Selectivity. *Inorg. Chem.* **2019**, *58*, 8517–8524.

(17) Li, K.; Peng, B.; Peng, T. Recent Advances in Heterogeneous Photocatalytic CO₂ Conversion to Solar Fuels. *ACS Catal.* **2016**, *6*, 7485–7527.

(18) Yang, W.; Wang, H. J.; Liu, R. R.; Zhang, C.; Li, C.; Zhong, D. C.; Lu, T. B. Tailoring crystal facets of metal-organic layers to enhance photocatalytic activity for CO₂ reduction. *Angew. Chem., Int. Ed.* **2021**, *60*, 409–414.

(19) Jiao, L.; Wang, Y.; Jiang, H.-L.; Xu, Q. Metal-Organic Frameworks as Platforms for Catalytic Applications. *Adv. Mater.* **2018**, *30*, 1703663–1703685.

(20) Kang, Y.-S.; Lu, Y.; Chen, K.; Zhao, Y.; Wang, P.; Sun, W.-Y. Metal-Organic Frameworks with Catalytic Centers: From Synthesis to Catalytic Application. *Coord. Chem. Rev.* **2019**, *378*, 262–280.

(21) Li, F. L.; Wang, P.; Huang, X.; Young, D. J.; Wang, H. F.; Braunstein, P.; Lang, J. P. Large-Scale, Bottom-Up Synthesis of Binary Metal-Organic Framework Nanosheets for Efficient Water Oxidation. *Angew. Chem., Int. Ed.* **2019**, *58*, 7051–7056.

(22) Liu, D.; Lang, J.-P.; Abrahams, B. F. Highly Efficient Separation of a Solid Mixture of Naphthalene and Anthracene by a Reusable Porous Metal-Organic Framework Through a Single-Crystal-to-Single-Crystal Transformation. *J. Am. Chem. Soc.* **2011**, *133*, 11042–11045.

(23) Li, F.-L.; Shao, Q.; Huang, X.; Lang, J.-P. Nanoscale Trimetallic Metal-Organic Framework Enable Efficient Oxygen Evolution Electroanalysis. *Angew. Chem., Int. Ed.* **2018**, *57*, 1888–1892.

(24) Liu, C.-Y.; Chen, X.-R.; Chen, H.-X.; Niu, Z.; Hirao, H.; Braunstein, P.; Lang, J.-P. Ultrafast Luminescent Light-Up Guest Detection Based on the Lock of the Host Molecular Vibration. *J. Am. Chem. Soc.* **2020**, *142*, 6690–6697.

(25) Liu, X.-Y.; Lo, W.-S.; Wu, C.; Williams, B. P.; Luo, L.; Li, Y.; Chou, L.-Y.; Lee, Y.; Tsung, C.-K. Tuning Metal-Organic Framework Nanocrystal Shape Through Facet-Dependent Coordination. *Nano Lett.* **2020**, *20*, 1774–1780.

(26) Liu, Q.; Jin, L.-N.; Sun, W.-Y. Facile Fabrication and Adsorption Property of a Nano/Microporous Coordination Polymer with Controllable Size and Morphology. *Chem. Commun.* **2012**, *48*, 8814–8816.

(27) Liu, Q.; Yang, J.-M.; Jin, L.-N.; Sun, W.-Y. Controlled Synthesis of Porous Coordination-Polymer Microcrystals with Definite Morphologies and Sizes under Mild Conditions. *Chem. —Eur. J.* **2014**, *20*, 14783–14789.

(28) Guo, F.; Guo, J.-H.; Wang, P.; Kang, Y.-S.; Liu, Y.; Zhao, J.; Sun, W.-Y. Facet-Dependent Photocatalytic Hydrogen Production of Metal-Organic Framework NH₂-MIL-125(Ti). *Chem. Sci.* **2019**, *10*, 4834–4838.

(29) Liu, H.; Zhang, J.; Ao, D. Construction of Heterostructured ZnIn₂S₄@NH₂-MIL-125(Ti) Nanocomposites for Visible-Light-Driven H₂ Production. *Appl. Catal., B* **2018**, *221*, 433–442.

(30) Li, S.; Ji, K.; Zhang, M.; He, C.; Wang, J.; Li, Z. Boosting the Photocatalytic CO₂ Reduction of Metal-Organic Frameworks by Encapsulating Carbon Dots. *Nanoscale* **2020**, *12*, 9533–9540.

(31) Li, L.; Wang, X. S.; Liu, T. F.; Ye, J. Titanium-Based MOF Materials: From Crystal Engineering to Photocatalysis. *Small Methods* **2020**, *4*, 2000486–2000514.

(32) Khaletskaya, K.; Pougin, A.; Medishetty, R.; Rösler, C.; Wiktor, C.; Strunk, J.; Fischer, R. A. Fabrication of Gold/Titania Photocatalyst for CO₂ Reduction Based on Pyrolytic Conversion of the Metal-Organic Framework NH₂-MIL-125(Ti) Loaded with Gold Nanoparticles. *Chem. Mater.* **2015**, *27*, 7248–7257.

(33) Yan, B.; Zhang, L.; Tang, Z.; Al-Mamun, M.; Zhao, H.; Su, X. Palladium-Decorated Hierarchical Titania Constructed from the Metal-Organic Frameworks NH₂-MIL-125(Ti) as a Robust Photocatalyst for Hydrogen Evolution. *Appl. Catal., B* **2017**, *218*, 743–750.

(34) Hu, J.; Ding, J.; Zhong, Q. In Situ Fabrication of Amorphous TiO₂/NH₂-MIL-125(Ti) for Enhanced Photocatalytic CO₂ into CH₄ with H₂O under Visible-Light Irradiation. *J. Colloid Interface Sci.* **2020**, *560*, 857–865.

(35) Li, N.; Liu, X.; Zhou, J.; Chen, W.; Liu, M. Encapsulating CuO Quantum Dots in MIL-125(Ti) Coupled with g-C₃N₄ for Efficient Photocatalytic CO₂ Reduction. *Chem. Eng. J.* **2020**, *399*, 125782–125792.

(36) Liu, S.; Yu, J.; Jaroniec, M. Anatase TiO₂ with Dominant High-Energy {001} Facets: Synthesis, Properties, and Applications. *Chem. Mater.* **2011**, *23*, 4085–4093.

(37) Smalley, A. P.; Reid, D. G.; Tan, J. C.; Lloyd, G. O. Alternative Synthetic Methodology for Amide Formation in the Post-Synthetic Modification of Ti-MIL125-NH₂. *CrystEngComm* **2013**, *15*, 9368–9371.

(38) Quan, Z.; Wang, Y.; Fang, J. High-Index Faceted Noble Metal Nanocrystals. *Acc. Chem. Res.* **2013**, *46*, 191–202.

(39) Kim, S.-N.; Kim, J.; Kim, H.-Y.; Cho, H.-Y.; Ahn, W.-S. Adsorption/Catalytic Properties of MIL-125 and NH₂-MIL-125. *Catal. Today* **2013**, *204*, 85–93.

(40) Melchionna, M.; Fornasiero, P. Updates on the Roadmap for Photocatalysis. *ACS Catal.* **2020**, *10*, 5493–5501.

(41) Beltram, A.; Romero-Ocaña, I.; José Delgado Jaen, J.; Montini, T.; Fornasiero, P. Photocatalytic Valorization of Ethanol and Glycerol over TiO₂ Polymorphs for Sustainable Hydrogen Production. *Appl. Catal., A* **2016**, *518*, 167–175.

(42) Huang, H.; Wang, X.-S.; Philo, D.; Ichihara, F.; Song, H.; Li, Y.; Li, D.; Qiu, T.; Wang, S.; Ye, J. Toward Visible-Light-Assisted Photocatalytic Nitrogen Fixation: A Titanium Metal Organic Framework with Functionalized Ligands. *Appl. Catal., B* **2020**, *267*, 118686–118692.

(43) Nasalevich, M. A.; Becker, R.; Ramos-Fernandez, E. V.; Castellanos, S.; Veber, S. L.; Fedin, M. V.; Kapteijn, F.; Reek, J. N. H.; van der Vlugt, J. I.; Gascon, J. Co@NH₂-MIL-125(Ti): Cobaloxime-Derived Metal-Organic Framework-Based Composite for Light-Driven H₂ Production. *Energy Environ. Sci.* **2015**, *8*, 364–375.

(44) Xiao, H.; Zhang, W.; Yao, Q.; Huang, L.; Chen, L.; Boury, B.; Chen, Z. Zn-free MOFs like MIL-53(Al) and MIL-125(Ti) for the Preparation of Defect-Rich, Ultrafine ZnO Nanosheets with High Photocatalytic Performance. *Appl. Catal., B* **2019**, *244*, 719–731.

(45) Chambers, M. B.; Wang, X.; Ellezani, L.; Ersen, O.; Fontecave, M.; Sanchez, C.; Rozes, L.; Mellot-Draznieks, C. Maximizing the Photocatalytic Activity of Metal-Organic Frameworks with Aminated-Functionalized Linkers: Substoichiometric Effects in MIL-125-NH₂. *J. Am. Chem. Soc.* **2017**, *139*, 8222–8228.

(46) Wang, S.; Xu, M.; Peng, T.; Zhang, C.; Li, T.; Hussain, I.; Wang, J. Y.; Tan, B. Porous Hypercrosslinked Polymer-TiO₂-Graphene Composite Photocatalysts for Visible-Light-Driven CO₂ Conversion. *Nat. Commun.* **2019**, *10*, 676–685.

(47) Wang, X.-K.; Liu, J.; Zhang, L.; Dong, L.-Z.; Li, S.-L.; Kan, Y.-H.; Li, D.-S.; Lan, Y.-Q. Monometallic Catalytic Models Hosted in

Stable Metal-Organic Frameworks for Tunable CO₂ Photoreduction. *ACS Catal.* **2019**, *9*, 1726–1732.

(48) Zhang, B.; Zhang, J.; Tan, X.; Shao, D.; Shi, J.; Zheng, L.; Zhang, J.; Yang, G.; Han, B. MIL-125-NH₂@TiO₂ Core-Shell Particles Produced by a Post-Solvothermal Route for High-Performance Photocatalytic H₂ Production. *ACS Appl. Mater. Interfaces* **2018**, *10*, 16418–16423.

(49) Lan, K.; Liu, Y.; Zhang, W.; Liu, Y.; Elzatahry, A.; Wang, R.; Xia, Y.; Al-Dhayan, D.; Zheng, N.; Zhao, D. Uniform Ordered Two-Dimensional Mesoporous TiO₂ Nanosheets from Hydrothermal-Induced Solvent-Confined Monomicelle Assembly. *J. Am. Chem. Soc.* **2018**, *140*, 4135–4143.

(50) Wang, H.; Yuan, X.; Wu, Y.; Zeng, X.; Leng, L.; Wu, Z.; Jiang, L.; Li, H. Facile Synthesis of Amino-Functionalized Titanium Metal-Organic Frameworks and Their Superior Visible-Light Photocatalytic Activity for Cr(VI) Reduction. *J. Hazard. Mater.* **2015**, *286*, 187–194.

(51) Zhou, M.; Wang, S.; Yang, P.; Huang, C.; Wang, X. Boron Carbon Nitride Semiconductors Decorated with CdS Nanoparticles for Photocatalytic Reduction of CO₂. *ACS Catal.* **2018**, *8*, 4928–4936.

(52) Xiang, Q.; Cheng, B.; Yu, J. Graphene-Based Photocatalysts for Solar-Fuel Generation. *Angew. Chem., Int. Ed.* **2015**, *54*, 11350–11366.